Measuring the Effects of Wake Steering With Nacelle-Mounted Scanning Lidar

Jacob A. Silverstein,[1,2] Julie K. Lundquist,[1,2,3]
Mithu Debnath,[1],[4] Eric Simley,[1] Alex Rybchuk[1]

1 National Renewable Energy Laboratory
2 University of Colorado Boulder
3 Renewable and Sustainable Energy Institute
4 AES Clean Energy

NREL is a national laboratory of the U.S. Department of Energy
Office of Energy Efficiency & Renewable Energy
Operated by the Alliance for Sustainable Energy, LLC

This report is available at no cost from the National Renewable Energy Laboratory (NREL) at www.nrel.gov/publications.

Contract No. DE-AC36-08GO28308

Technical Report
NREL/TP-5000-87776
April 2024

Measuring the Effects of Wake Steering With Nacelle-Mounted Scanning Lidar

Jacob A. Silverstein,[1,2] Julie K. Lundquist,[1,2,3]
Mithu Debnath,[1,4] Eric Simley,[1] Alex Rybchuk[1]

1 National Renewable Energy Laboratory
2 University of Colorado Boulder
3 Renewable and Sustainable Energy Institute
4 AES Clean Energy

Suggested Citation
Silverstein, Jacob A., Julie K. Lundquist, Mithu Debnath, Eric Simley, and Alex Rybchuk. 2024. *Measuring the Effects of Wake Steering With Nacelle-Mounted Scanning Lidar*. Golden, CO: National Renewable Energy Laboratory. NREL/TP-5000-87776. https://www.nrel.gov/docs/fy24osti/87776.pdf.

NREL is a national laboratory of the U.S. Department of Energy
Office of Energy Efficiency & Renewable Energy
Operated by the Alliance for Sustainable Energy, LLC

This report is available at no cost from the National Renewable Energy Laboratory (NREL) at www.nrel.gov/publications.

Contract No. DE-AC36-08GO28308

Technical Report
NREL/TP-5000-87776
April 2024

National Renewable Energy Laboratory
15013 Denver West Parkway
Golden, CO 80401
303-275-3000 • www.nrel.gov

NOTICE

This work was authored in part by the National Renewable Energy Laboratory, operated by Alliance for Sustainable Energy, LLC, for the U.S. Department of Energy (DOE) under Contract No. DE-AC36-08GO28308. Funding provided by the U.S. Department of Energy Office of Energy Efficiency and Renewable Energy Wind Energy Technologies Office. The views expressed herein do not necessarily represent the views of the DOE or the U.S. Government.

Cover Photos by Dennis Schroeder: (clockwise, left to right) NREL 51934, NREL 45897, NREL 42160, NREL 45891, NREL 48097, NREL 46526.

Table of Contents

List of Acronyms . . . . . **iv**

Executive Summary . . . . . **v**

1 Introduction **1**

2 Site Layout and Instruments **2**

2.1 Stability, Turbulence, and Wind Characteristics 3

2.2 Wake Steering Controller 5

3 Data Preprocessing and Analysis Methodology **7**

3.1 Clean Primary Data (QC_1) 7

3.2 Fit Model to Cleaned Data (QC_2) 7

3.3 Validate Model Fitness (QC_3) 8

4 Results **10**

4.1 General Model Performance and Overall Trends of Wake Behavior 10

4.2 Wake Characteristics As a Function of Turbine Operating Condition 11

4.3 Wake Deficits As a Function of Atmospheric Stability and Turbulence Intensity 12

4.4 Wake Widths As a Function of Atmospheric Stability and Turbulence Intensity 13

4.5 Wake Centerlines As a Function of Atmospheric Stability and Turbulence Intensity 13

5 Discussion and Conclusions **16**

References **20**

List of Figures

Figure 1. Layout and locations of the instruments with reference to the target turbine T2. Contour color of the figure represents the terrain height of the site. 2

Figure 2. Lidar scans at elevation angle of zero for (a) a yawed wake in a wide scan and (b) an unyawed wake in a narrow scan. The lidar is located at $x = 0$, $y = 0$, and the data are plotted with nacelle line-of-sight wind speed, U_{LOS}, frame of reference. The wind flows from left to right. 3

Figure 3. Distribution of the atmospheric stability parameter, $\zeta = z/L$, measured at 10 m for the duration of the experiment, July 2019–February 2020. 4

Figure 4. Turbulence intensity at 60 m measured by the cup anemometer versus stability parameter, ζ, measured at 10 m. Dashed orange lines represent 8% turbulence intensity and $\zeta = 0$. 4

Figure 5. Distribution of (a) TI at 60-m height (as measured by the 1-Hz cup anemometer) and (b) wind speed (as measured by the ground-based profiling lidar) by turbine operating condition. 5

Figure 6. Wake steering controller. 5

Figure 7. Target yaw offsets for wake steering for turbine T2 as a function of wind direction and wind speed (u). 6

Figure 8. Data processing pipeline for quality control (stages QC_1 through QC_3). 7

Figure 9. Examples of fitted line-of-sight lidar data using (a) a single-Gaussian curve at $3D$ downwind, (b) a double-Gaussian curve at $3D$ downwind, (c) a single-Gaussian curve at $5D$ downwind, and (d) a double-Gaussian curve at $5D$ downwind to model the observations. 8

Figure 10. Modeled ambient wind speed versus measured ambient wind speed, in which modeled ambient winds come from (a) single-Gaussian and (b) double-Gaussian curve fits. 9

Figure 11. Estimates from the fitted model for (a) ambient wind speed, (b) velocity deficit, (c) wake width, and (d) wake center across all downwind range gates. The shaded regions denote one standard deviation, σ, and dashed lines represent available number of scans at each downrange location. 10

Figure 12. (a, c, e) Wake behavior for all cases under different turbine operating regions, and (b, d, f) a comparison of yawed and unyawed behavior for cases occurring in Regions 2 and 2.5. Note that yawing was inactive in turbine operating Region 3, so the corresponding unyawed data are omitted from the comparison. Any statistically significant differences are highlighted at each range gate with a diamond marker. . . 11

Figure 13. Velocity deficits of yawed and unyawed wakes under (a, b) different atmospheric stability regimes and (c, d) turbulence intensity conditions. Note that solid lines represent the mean of all cases, and dashed lines represent available number of scans. Any statistically significant differences are highlighted at each range gate with a diamond marker. 12

Figure 14. Wake widths of yawed and unyawed wakes under (a, b) different atmospheric stability regimes and (c, d) turbulence intensity conditions. Note that solid lines represent the mean of all cases, and dashed lines represent available number of scans. Any statistically significant differences are highlighted at each range gate with a diamond marker. 14

Figure 15. Wake centers of yawed and unyawed wakes under (a) stable atmospheric conditions, (b) unstable atmospheric conditions, (c) low turbulence intensity, and (d) high turbulence intensity. Solid lines represent the mean of all cases, and dashed lines represent available number of scans. Any statistically significant differences are highlighted at each range gate with a diamond marker. 15

List of Tables

Table 1. Classification of the Atmospheric Boundary Layer Stability Regimes Using the Stability Parameter $\zeta = z/L$ where z is the height of the sonic anemometer at 10 m. 3

List of Acronyms

ABL	Atmospheric Boundary Layer
LES	Large-eddy Simulation
FLORIS	FLOw Redirection and Induction in Steady State
TI	Turbulence Intensity
QC	Quality Control

Executive Summary

In large wind plants, wakes from upwind turbines affect downwind turbines by reducing wind speeds and increasing turbulence. Wake steering may mitigate this effect by deflecting the wakes of upwind turbines away from downwind units. Here, we characterize the impact of wakes from yawed turbines at a commercial-scale wind plant under varying atmospheric and turbine operating conditions. Six months of nacelle-based lidar measurements were collected as part of a field campaign in 2019–2020 in the northern U.S. Great Plains to test the effectiveness of wake steering. We separate these lidar scans by atmospheric stability and turbine operating condition to summarize how yawed wind turbine wakes vary with these input parameters in the atmospheric boundary layer. We summarize the impact of wake steering on various wake characteristics, including velocity deficit, wake width, and wake center as retrieved from these lidar data. Yawed wakes have significantly different centerline characteristics compared to unyawed wakes, with larger regions of deflection in the midwake region. Yawed wakes are also deflected farther in less turbulent conditions. Velocity deficits persist farther downstream in stable atmospheric conditions compared with unstable atmospheric conditions regardless of whether or not turbines are aligned to the mean wind direction. Overall, yawed wind turbine wakes are larger and wider in slower wind speed environments, yawed wake velocity deficits are smaller than unyawed wake velocity deficits in unstable conditions, and yawed wakes are deflected farther in stable atmospheric conditions. These findings suggest that wake steering is most effective in stable atmospheric stratification.

1 Introduction

Wind turbines within a wind plant affect each other. They generate wakes that slow wind speeds and increase turbulence. In a wind plant, wakes from upstream turbines degrade the performance of downwind turbines and decrease overall power production (Lissaman 1979; Thomson and Sorensen 1999; Porté-Agel, Bastankhah, and Shamsoddin 2020). For example, wakes reduce annual energy production by between 5% and 40% (Lee and Fields 2021).

Wind plant flow control may combat negative impacts from wakes. A number of control strategies have been proposed (Meyers et al. 2022). Among these, static yaw control is likely the most mature technique and closest to widespread adoption by commercial plants (e.g., Siemens Gamesa Renewable Energy 2019; Fleming et al. 2017a; Fleming et al. 2019; Fleming et al. 2020). Under typical operation, each turbine in a plant aligns its rotor disk with the direction of incoming wind. Under static yaw control, an upwind turbine is intentionally yawed away from the direction of background flow so that the wake is horizontally deflected and steered away from downwind turbines.

Before yaw control can be widely adopted as standard practice in industry, it is important to thoroughly characterize the dynamics of the controlled wakes so that their impacts can accurately be assessed. Confidence in yaw control has been increasing through high-fidelity modeling with tools like large-eddy simulation (LES) (Machefaux et al. 2016; Archer and Vasel-Be-Hagh 2019), small-scale testing in a wind tunnel (Bastankhah and Porté-Agel 2016; Shapiro, Gayme, and Meneveau 2018), and full-scale testing on industrial turbines (Aitken and Lundquist 2014; Brugger et al. 2020).

While trust in yaw control has grown, lack of validation represents one of the largest hurdles to widespread commercial implementation (Wingerden et al. 2020). Validation on full-scale turbines is particularly important for eventual commercial implementation. Previous commercial-scale yaw control studies (Fleming et al. 2017b; Fleming et al. 2020; Ahmad et al. 2019; Howland, Lele, and Dabiri 2019; Doekemeijer et al. 2021; Simley et al. 2021) have focused on power production as their quantity of interest. In contrast, engineering models of yawed wakes that would be used for flow control (e.g., Martínez-Tossas et al. 2019; Shapiro et al. 2019; King et al. 2021; Bastankhah et al. 2022; Sengers et al. 2022) directly predict wind speed deficits, which are in turn used to predict power production. Thus, while power measurements from industrial-scale studies are useful for validation, model validation efforts would be aided by measurements of wind speeds in wakes. In this paper, we focus on open questions pertaining to interactions between wind energy and the atmosphere, such as (1) How do yawed wakes differ from unyawed wakes? (2) How does atmospheric stability impact yawed wakes? (3) How does yaw control impact measured wind speeds at a wind plant?

This report is structured as follows: in Section 2, we describe the site layout and instruments used to gather data. Section 2.1 describes the wind characteristics of the site, and Section 2.2 provides information about steering the turbine. Section 3 describes the methods used to quality-check and model the nacelle-mounted lidar data. In order to analyze measurements, we first develop an extensive quality control technique to filter out inadequate data. This is followed by our results in Section 4, where we partition our analysis to examine measured wake behavior as a function of wind speed (which dictates the operating region of the power curve), atmospheric stability, and turbulence intensity. We additionally characterize yaw control on the effect of average wake geometry (i.e., the wake centerline location and wake width). Finally, our conclusions are presented in Section 5.

2 Site Layout and Instruments

The data for this study were collected during a field campaign that spanned July 2019 to February 2020 in a subsection of a commercial-scale wind plant in the northern U.S. Great Plains (Fleming et al. 2019; Murphy, Lundquist, and Fleming 2020; Brugger et al. 2020). Wind speed data were measured by nacelle-mounted scanning lidars coupled with meteorological (met) tower instrumentation for quantifying atmospheric stability. The layout of the turbines and terrain of the site appear in Figure 1. All turbines are General Electric 1.5-MW super-long extended cold-weather extreme models, each with a hub height of 80 m, rotor diameter, D, of 77 m, cut-in speed of 3.5 m s^{-1}, cut-out speed of 25 m s^{-1}, and a rated wind speed of 14 m s^{-1} (Murphy, Lundquist, and Fleming 2020). Due to the presence of complex terrain south of the turbines (Figure 1), only northerly wind direction and wakes from turbine T2 are investigated in this study.

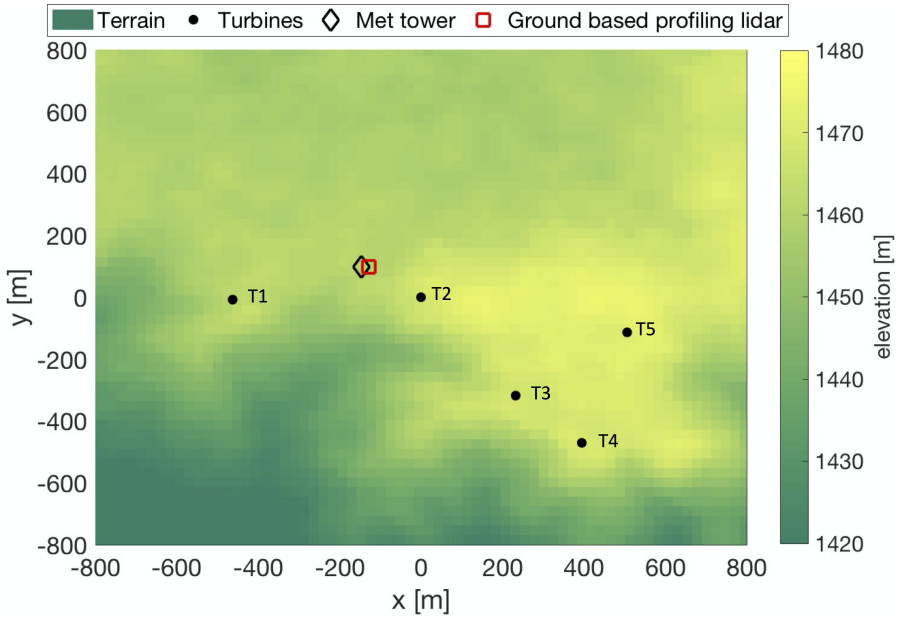

Figure 1. Layout and locations of the instruments with reference to the target turbine T2. Contour color of the figure represents the terrain height of the site.

A Galion-4000 scanning lidar (Wang et al. 2015) was mounted in a fixed position on the nacelle of T2 to measure downwind of the turbine. In the coordinate system used in this analysis, 0° azimuth (θ) represents the lidar looking directly upwind, parallel to the nacelle and perpendicular to the turbine rotor disk, and 180° azimuth (θ) represents the downwind line of sight of the lidar parallel to the nacelle. Two types of scans were conducted each hour: 30 minutes were assigned to a narrow-sector scan of azimuth 163° to 193° with angular resolution of 3°, and 30 minutes were assigned to a wider sector of azimuth 163° to 220°, also with an angular resolution of 3°. The range gate resolution of the scans was approximately 18 m. The scans were designed to capture the full wake at a distance of 2.5D downwind, so wake characterization in the near wake is not possible.

Narrow scans captured wakes when the turbine was aligned with the mean wind direction, and wider scans are targeted for the steered wakes. Only scans with elevation angles (ϕ) of 0° are considered here in order to focus on hub-height wind speeds. Wakes appear as distinct areas containing slower wind speeds as measured by the lidar. Sample scans with wide and narrow sectors are presented in Figure 2, in which panel (a) shows a steered wake while panel (b) shows an aligned wake.

The lidar measures wind speeds along the line of sight, denoted as $U_{LOS}(r)$. As in Aitken and Lundquist (2014), the line-of-sight velocity from a lidar is a function of the complete horizontal wind speed U, the azimuth angle of the lidar θ, and the yaw angle ϕ, where the elevation angle is assumed to be zero:

$$U_{\mathrm{LOS}}(r) = U\cos(\theta+\phi). \tag{2.1}$$

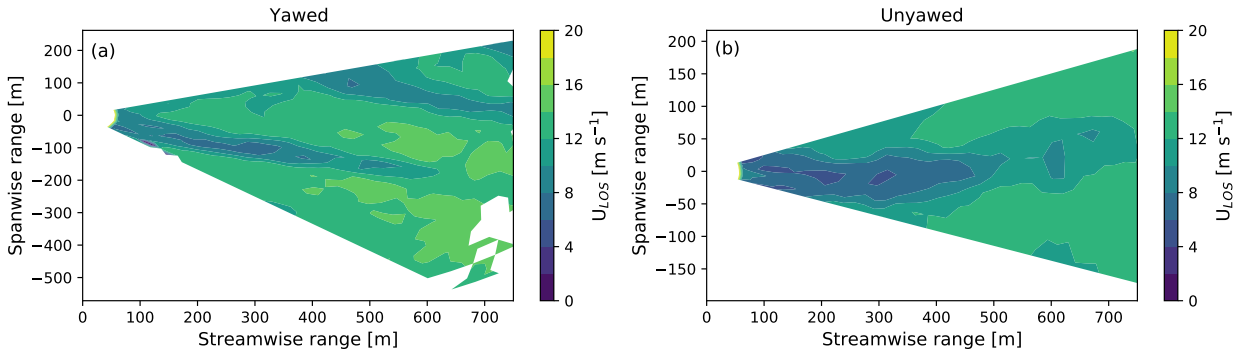

Figure 2. Lidar scans at elevation angle of zero for (a) a yawed wake in a wide scan and (b) an unyawed wake in a narrow scan. The lidar is located at $x = 0, y = 0$, and the data are plotted with nacelle line-of-sight wind speed, U_{LOS}, frame of reference. The wind flows from left to right.

The angle between the lidar beam and the vector describing the wind field at a given point is $\theta + \phi$.

2.1 Stability, Turbulence, and Wind Characteristics

A 60-m tall met tower installed 178 m northwest of the T2 turbine characterizes the atmospheric conditions. The met tower has a Class 1 cup anemometer at a height of 60 m, a Campbell Scientific CSAT3 sonic anemometer at 10 m, and pressure, humidity, and temperature sensors installed at 3 m. The Obukhov length at 10-m height is calculated as:

$$L = -\frac{u_\star^3 T_v}{kg\overline{w'T_s'}}, \tag{2.2}$$

where $u_\star$ is friction velocity, $k = 0.4$ is the von Kármán constant, T_v is virtual temperature, g is the force of gravity, and $\overline{w'T_s'}$ is the kinematic heat flux. Fluxes are calculated from the 20-Hz sonic anemometer data using a moving window of 30 minutes followed by resampling every 10 minutes.

Table 1. Classification of the Atmospheric Boundary Layer Stability Regimes Using the Stability Parameter $\zeta = z/L$ where z is the height of the sonic anemometer at 10 m.

Stability Class	ζ	Percent of data (%)
Unstable/ Convective	$-2 < \zeta < -0.01$	45.2
Neutral	$-0.01 < \zeta < 0.01$	7.1
Stable	$0.01 < \zeta < 2$	47.6

The atmospheric boundary layer (ABL) is classified into neutral, unstable, and stable conditions using the stability parameter, $\zeta \equiv z/L$ following Murphy, Lundquist, and Fleming (2020). We denote $-2 < \zeta < -0.01$ as unstable, $-0.01 < \zeta < 0.01$ as neutral, and $0.01 < \zeta < 2$ as stable. About 45% of cases are unstable while about 48% of the data represented stable conditions. As is typical in the northern Great Plains, very few neutral conditions occur (Vanderwende and Lundquist 2012; Murphy, Lundquist, and Fleming 2020): just over 7% of the stability data are considered neutral (Figure 3). Unlike Murphy, Lundquist, and Fleming (2020), we limit our data set to $\pm$ 2 rather than $\pm\infty$. Due to the small data set, the neutral data are not considered in this analysis.

The 1-Hz cup anemometer data are used to calculate turbulence intensity (TI) at 60-m height. The cup anemometer and a wind vane provide horizontal wind speed and wind direction measurements at 60 m and 56 m, respectively. TI is calculated as the 10-minute averaged standard deviation of the wind speed divided by the 10-minute mean, after a linear detrending of the 10-minute window is applied (Fleming et al. 2019). The turbulence intensity at 60 m varies with atmospheric stability conditions (Figure 4). The median TI is large (15%) in unstable ABL conditions and small (5%) in stable ABL conditions. The median TI for neutral cases is approximately 8% and is used to separate low- and high-TI conditions. Using this division, about 45% of the data fell into the high-TI range, and about 54% of the data fell into the low-TI range (Figure 5a). Due to the small size of the data set, we did not filter out data to account

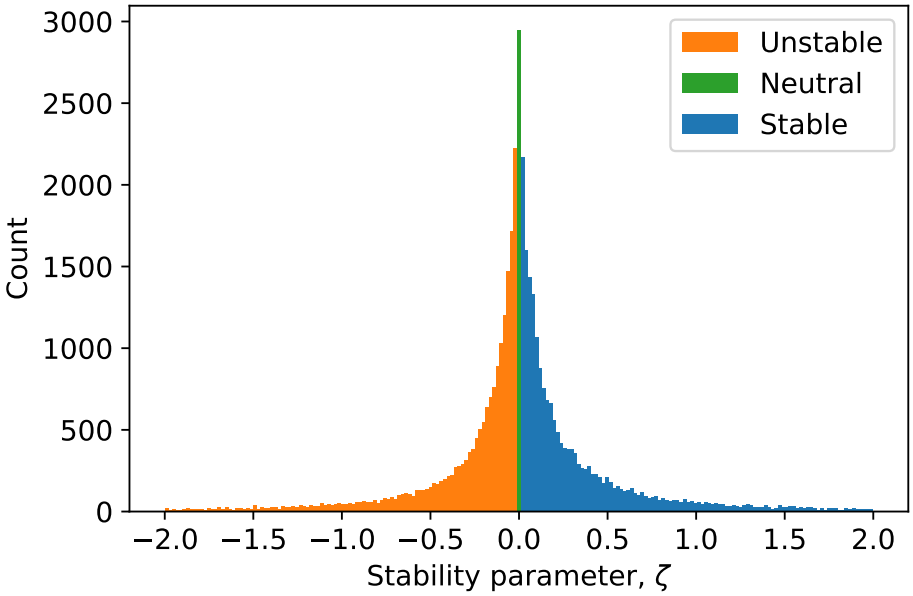

Figure 3. Distribution of the atmospheric stability parameter, $\zeta = z/L$, measured at 10 m for the duration of the experiment, July 2019–February 2020.

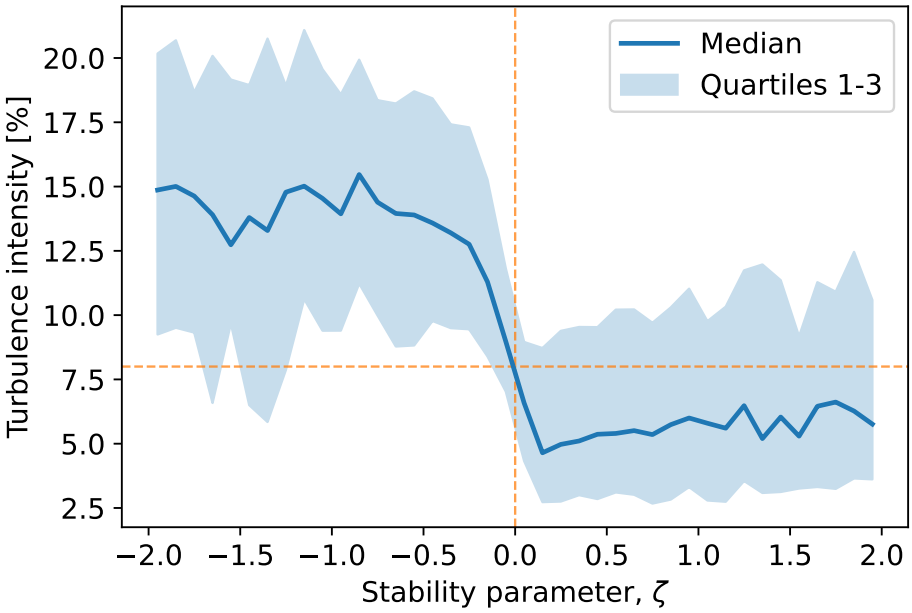

Figure 4. Turbulence intensity at 60 m measured by the cup anemometer versus stability parameter, ζ, measured at 10 m. Dashed orange lines represent 8% turbulence intensity and $\zeta = 0$.

for any tower waking. The sonics are used in a coarse manner: e.g., to check if the atmosphere is either stable or unstable, low TI or high TI.

A ground-based profiling lidar (Windcube v2) located near the met tower provides wind speed and direction at hub height. The lidar measures wind speed at approximately 1 Hz from heights of 40 m to 200 m with 20-m vertical resolution. Wind speeds measured by the profiling lidar at 80 m are divided into three regions following the operating regimes of the wind turbines at this site. Wind speeds between 2.5 and 9 m s^{-1} are considered Region 2, in which the turbine has a large thrust coefficient. Wind speeds between 9 and 14 m s^{-1} are considered Region 2.5, in which the blades begin to pitch. Finally, speeds between 14 and 25 m s^{-1} define Region 3, in which the blades are pitched and

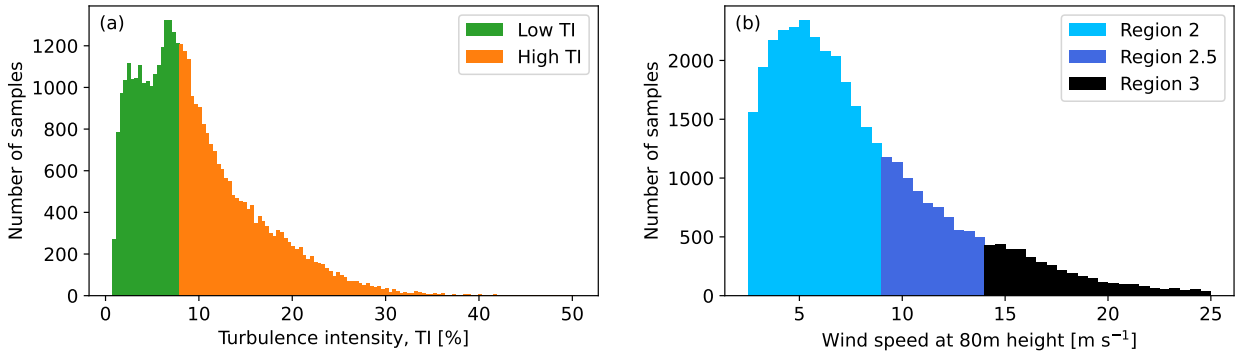

Figure 5. Distribution of (a) TI at 60-m height (as measured by the 1-Hz cup anemometer) and (b) wind speed (as measured by the ground-based profiling lidar) by turbine operating condition.

the thrust coefficient may be small. In this data set, slightly more than 73% of the data occur in Region 2; Regions 2.5 and 3 have approximately 12% and 14% of data, respectively (Figure 5b).

2.2 Wake Steering Controller

Wake steering is implemented by modifying the wind vane input to the turbine's existing yaw controller using the control structure shown in Figure 6. Detailed information about the wake steering control strategy can be found in Fleming et al. (2019) and Fleming et al. (2020), but basic details are presented here. Target yaw offsets are determined as a function of wind direction and wind speed, where the wind direction is calculated by adding the relative wind direction measured by the nacelle wind vane to the turbine's absolute yaw position. The wind direction and wind speed signals are then filtered using low-pass filters with time constants of 30 s and 60 s, respectively, to remove high-frequency variations that are not relevant for wake steering. Next, a lookup table is used to determine a target yaw offset from the filtered wind direction and wind speed signals. Finally, the measured nacelle wind vane signal is modified by subtracting the target yaw offset before it is sent to the turbine's yaw controller, thereby inducing the intended yaw offset. To allow wake steering to be compared to baseline yaw control in similar sets of wind conditions, the controller toggles hourly between standard yaw control (no offset) and wake steering control. The yaw offsets are updated at a rate of 1 Hz.

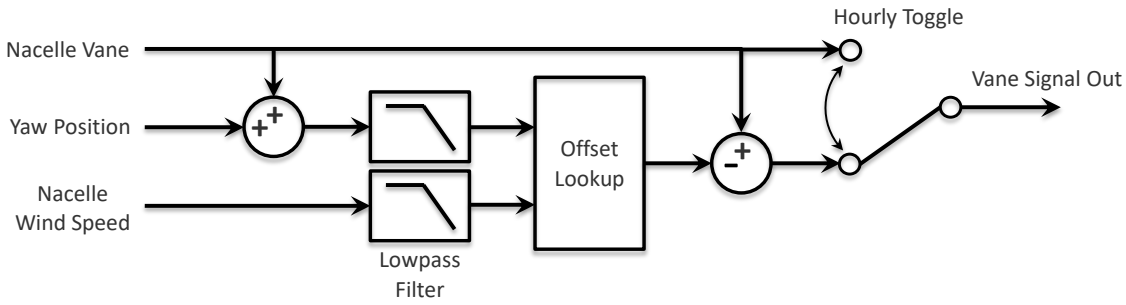

Figure 6. Wake steering controller.

The target yaw offsets that make up the lookup table at the core of the wake steering controller are shown in Figure 7 as a function of wind direction and wind speed. The yaw offsets are a simplified form of the optimal offsets for maximizing the combined power of turbines T2 and T3 for wind speeds below 9.5 m s^{-1} determined using the FLOw Redirection and Induction in Steady State (FLORIS) engineering wind farm control tool (NREL 2021). Further, to account for variable wind conditions and relatively slow yaw control dynamics, the offsets were optimized considering some robustness to wind direction uncertainty. The target yaw offsets are constrained to be positive (a counterclockwise rotation of the nacelle relative to the wind direction when viewed from above) because (1) negative offsets can cause higher structural loads, as shown by Damiani et al. (2018), and (2) large-eddy simulation (LES) studies suggest that positive offsets can yield a greater increase in power (Fleming et al. 2018; Nouri, Vasel-Be-Hagh, and Archer 2020). Additionally, to maintain acceptable structural loading, the yaw offsets are limited to 20°

for wind speeds below 9.5 m s^{-1}, with a gradually decreasing upper bound as wind speed increases from 9.5 m s^{-1} to 14.5 m s^{-1}. The target offsets are reduced to zero for wind speeds above 14.5 m s^{-1}.

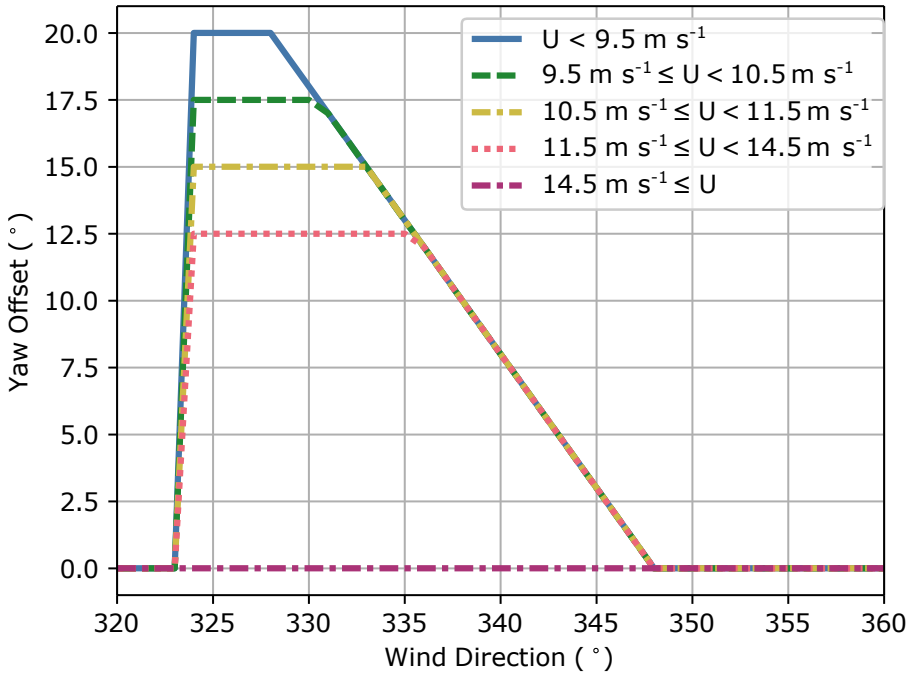

Figure 7. Target yaw offsets for wake steering for turbine T2 as a function of wind direction and wind speed (u).

3 Data Preprocessing and Analysis Methodology

The three data sets (lidar, met tower, and wind vane) are synchronized and used to filter out low-quality data, as summarized in Figure 8.

3.1 Clean Primary Data (QC_1)

In step 1 (QC_1), the signal-to-noise ratio (SNR) of the return signal is used to remove low-quality lidar data. The line-of-sight wind speed data are only considered for the corresponding SNR from 5 dB to -18 dB. Additionally, negative line-of-sight wind speed data are removed to account for errors in the lidar measurements, as it is deemed nonphysical for there to be a reversal in wake velocity. This step removed 7,968 range gates ($\approx 1\%$) from the data set. For missing data at each downwind range gate distance, all the data downwind of that point for that scan are also disregarded to exclude any possible low-quality data farther downstream. This step removed 244,798 range gates ($\approx 30\%$) from the data set. Together, these two processes in QC_1 removed 252,766 range gates ($\approx 31\%$) out of the total 821,844 range gates in the full lidar data set.

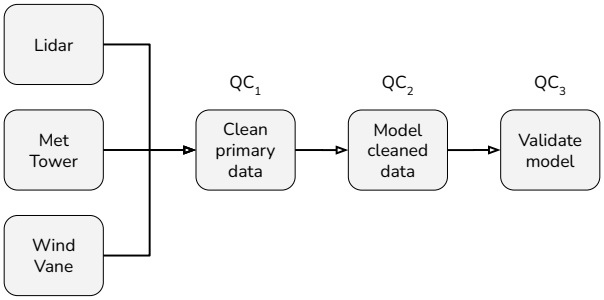

Figure 8. Data processing pipeline for quality control (stages QC_1 through QC_3).

Before fitting the lidar data with the Gaussian model, the number of unavailable data points at each downwind location is checked. The fitting of a Gaussian model at a downwind range is only considered if the number of unavailable data points is less than two, and the considered unavailable data point is replaced with a cubic curve fitting of the available data. Furthermore, a backward linear interpolation method is used to replace the first data point in the array if it is unavailable.

3.2 Fit Model to Cleaned Data (QC_2)

A Gaussian model is fitted to the nacelle-based lidar data (as retrieved at the lidar's line of sight). This is performed individually at each of the 12 downwind range gates for every scan, as in Aitken and Lundquist (2014) and Bodini, Zardi, and Lundquist (2017):

$$U_{LOS}(y',r) = \left(U - a\exp\left[\frac{-(y'-y_c)^2}{2s_w^2}\right]\right)\left(\frac{\sqrt{r^2-y'^2}}{r}cos\phi + \frac{y'}{r}sin\phi\right), \tag{3.1}$$

where the amplitude of the wake (which represents the wake deficit) is denoted by a, wake width is denoted by s_w, y' is the spanwise distance, y_c is wake centerline, r is distance along the line of sight, and ϕ is yaw angle of the turbine in counterclockwise rotation. The actual wake width based on the curve fitting is given by:

$$w = 4s_w. \tag{3.2}$$

Additionally, a double-Gaussian model is fitted to the line-of-sight wind speed data as measured by the lidar over the same 12 downwind range gates, as in Aitken and Lundquist (2014) and Bodini, Zardi, and Lundquist (2017):

$$U_{LOS}(y',r) = \left(U - a\{\exp\left[\frac{-(y'-y_l)^2}{2s_w^2}\right] + \exp\left[\frac{-(y'-y_r)^2}{2s_w^2}\right]\}\right)\left(\frac{\sqrt{r^2-y'^2}}{r}cos\phi + \frac{y'}{r}sin\phi\right), \tag{3.3}$$

where y_l and y_r are used respectively instead of y_c. Wake velocity deficit (VD) is normalized according to the ambient wind speed by:

$$VD = \frac{a}{U} \cdot 100\%. \tag{3.4}$$

To determine whether to select a single-Gaussian or double-Gaussian fit for each case, we perform an extra sum-of-squares F-test as in Aitken and Lundquist (2014). If the p-value output by the test was less than a set threshold value of $\alpha = 0.05$, then we reject the simpler model and use our double-Gaussian fit. In QC_2, data from individual hub-height scans used in the Gaussian-model fitting process that passed the QC_1 step are modeled to the lidar data using Equation (3.1) and Equation (3.3) for the line-of-sight wind speed. Figure 9 shows both of the models fitted at select downwind range gate distances with single-Gaussian fits on the left and double-Gaussian fits on the right.

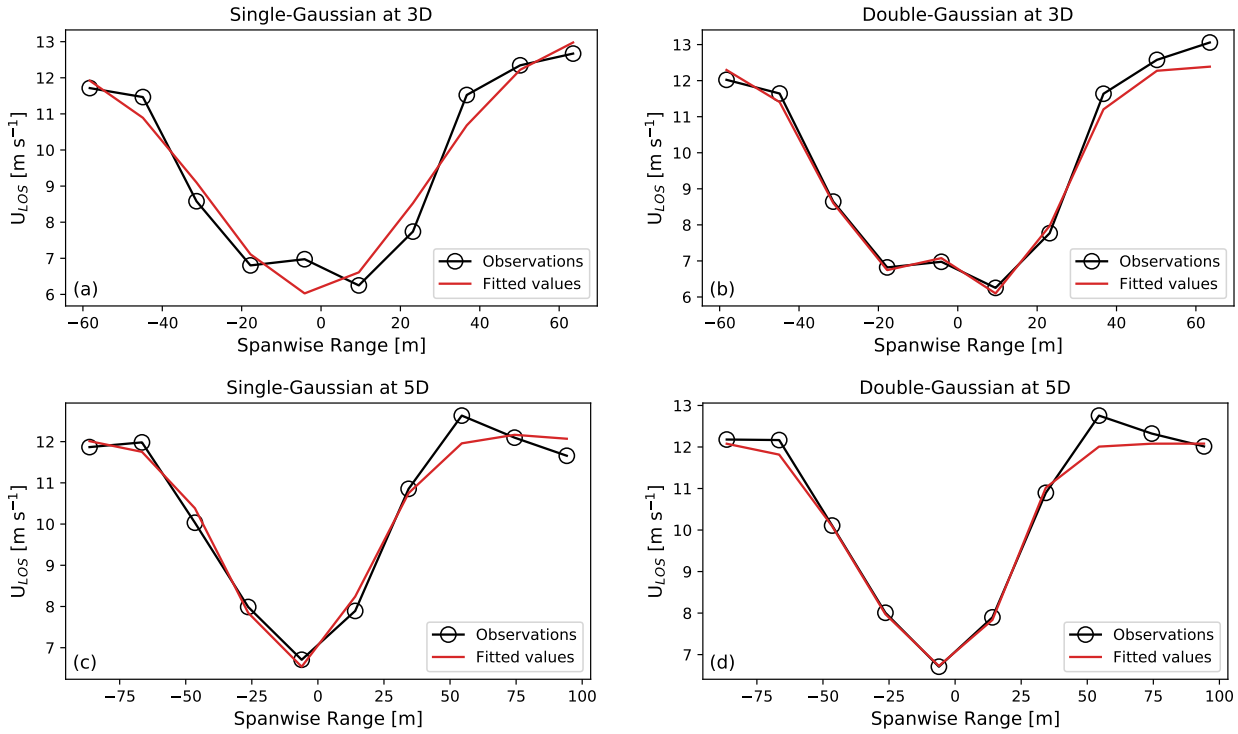

Figure 9. Examples of fitted line-of-sight lidar data using (a) a single-Gaussian curve at $3D$ downwind, (b) a double-Gaussian curve at $3D$ downwind, (c) a single-Gaussian curve at $5D$ downwind, and (d) a double-Gaussian curve at $5D$ downwind to model the observations.

Parameters from the model are extracted to examine various wake characteristics such as velocity deficit, wake width, and centerline location. We will further discuss wake characteristics in terms of velocity deficit and wake recovery. Velocity deficit refers to the amplitude of the curve, which is denoted as a in Equation (3.1) and Equation (3.3). Wake recovery refers to the decrease in velocity deficit that occurs as wakes mix with ambient winds while moving downstream such that the deficit decreases.

3.3 Validate Model Fitness (QC_3)

To avoid spurious predictions made by the curve-fitting model, a series of constraints are added to the curve-fitting process. If the model's wake velocity deficit is negative, or if the model's ambient wind speed is larger than the measured wind speed at 80-m height, or the model's wake width is unreasonable (less than 40 m or greater than 300

m for $D = 77$ m), the fitted data are not considered. This quality control process is denoted as QC step 3 (QC_3). This step flagged and removed 366,606 range gates ($\approx 45\%$) from the data set.

To verify the models, we compare ambient wind measurements from the profiling lidar to predictions of modeled ambient wind speed from Gaussian fits to scanning lidar data. Figure 10 shows predicted ambient wind speed with respect to the wind speed data retrieved at 80-m height as measured by the profiling lidar. We assume an approximately normal distribution of measured data. The single-Gaussian model's performance is shown in Figure 10a, and the double-Gaussian model's performance is shown in Figure 10b. The target fit line represents what a near perfect fit of the data looks like, where measured wind speed and modeled wind speed are equivalent.

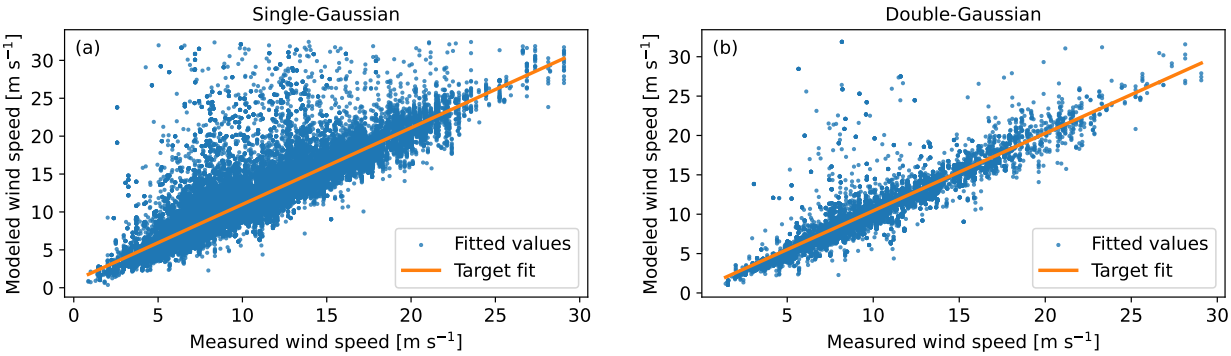

Figure 10. Modeled ambient wind speed versus measured ambient wind speed, in which modeled ambient winds come from (a) single-Gaussian and (b) double-Gaussian curve fits.

Overall, 202,472 range gates out of the original 821,844 passed the quality control pipeline, indicating an acceptance rate of $\approx 24.6\%$ of the data. After the quality control process, the fitted lidar data and corresponding atmospheric data are saved for conditional analysis.

4 Results

4.1 General Model Performance and Overall Trends of Wake Behavior

Before discussing the impact of wake steering, we first evaluate both yawed and unyawed measurements together in order to give a general view of our model's performance. We note that the distributions across all target parameters in the model are similar whether scans are summarized by their mean or median (Figure 11). As such, we use the mean for the remaining analysis in this section in order to encapsulate any statistically significant differences between our target classes. Differences between groups are calculated by performing a Welch's T-test at each range gate. Note that as downwind distance increases, the available number of scans decreases due to lidar signal attenuation.

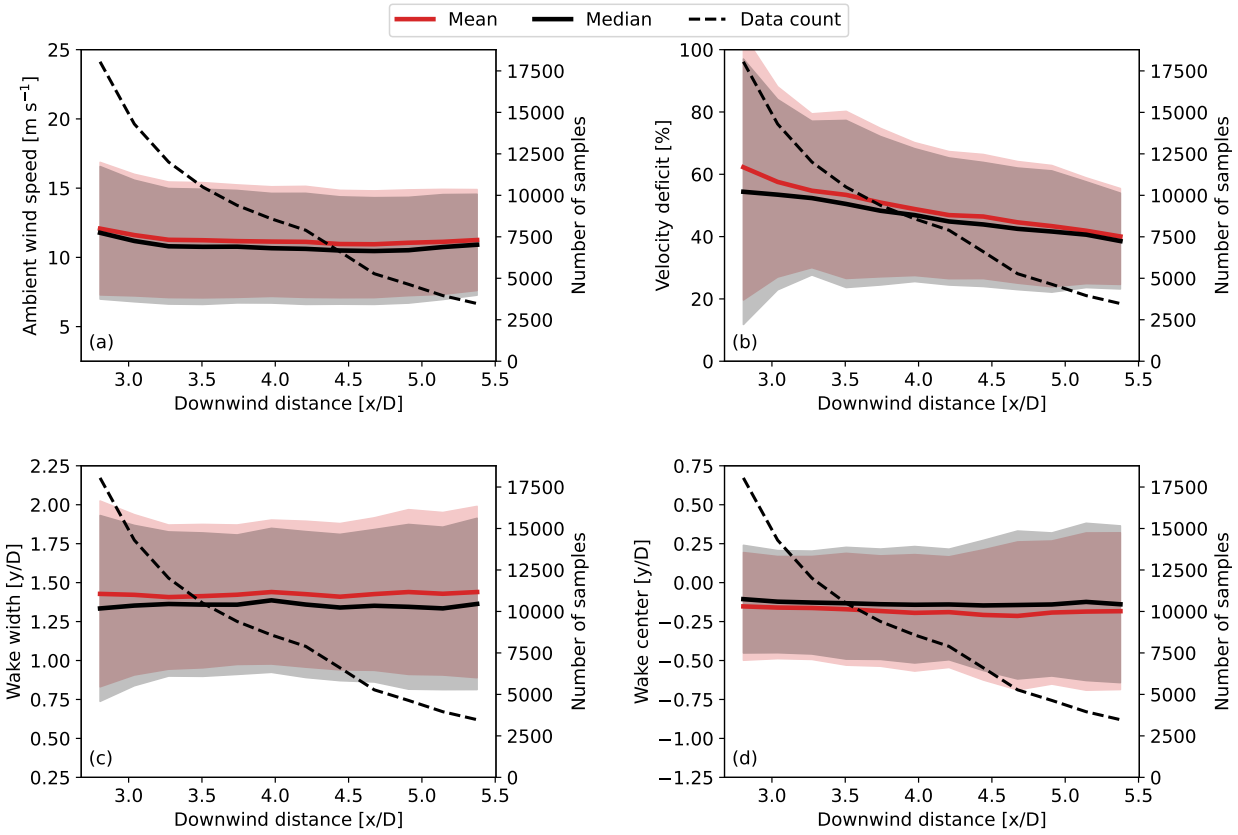

Figure 11. Estimates from the fitted model for (a) ambient wind speed, (b) velocity deficit, (c) wake width, and (d) wake center across all downwind range gates. The shaded regions denote one standard deviation, σ, and dashed lines represent available number of scans at each downrange location.

Looking across all cases, the mean wake velocity deficit is $\approx 55\%$ at $3D$ downstream distance and $\approx 45\%$ at $5.3D$ downstream distance, which is generally consistent with previous studies (Aitken et al. 2014). The mean velocity deficit generally decreases with increasing distance away from the turbine, and wakes recover as we move farther downwind. As is the case for the mean velocity deficit, the standard deviation of the velocity deficits generally decreases when moving downwind.

We note that the mean wake center across all data is not located at $y/D = 0.0$ as would be expected, but it instead sits near $y/D = 0.125$ (Figure 11d). This offset could stem from a number of factors: misalignment between the lidar azimuth with respect to the rotor axis, miscalibration between the yaw measurement system and true north, and a possible non-zero yaw offset during baseline operations. It is unclear which of these factors produces the offset. However, even with this offset, we are able to compare the relative behavior of yawed and unyawed wakes and discern a meaningful difference in the following analysis.

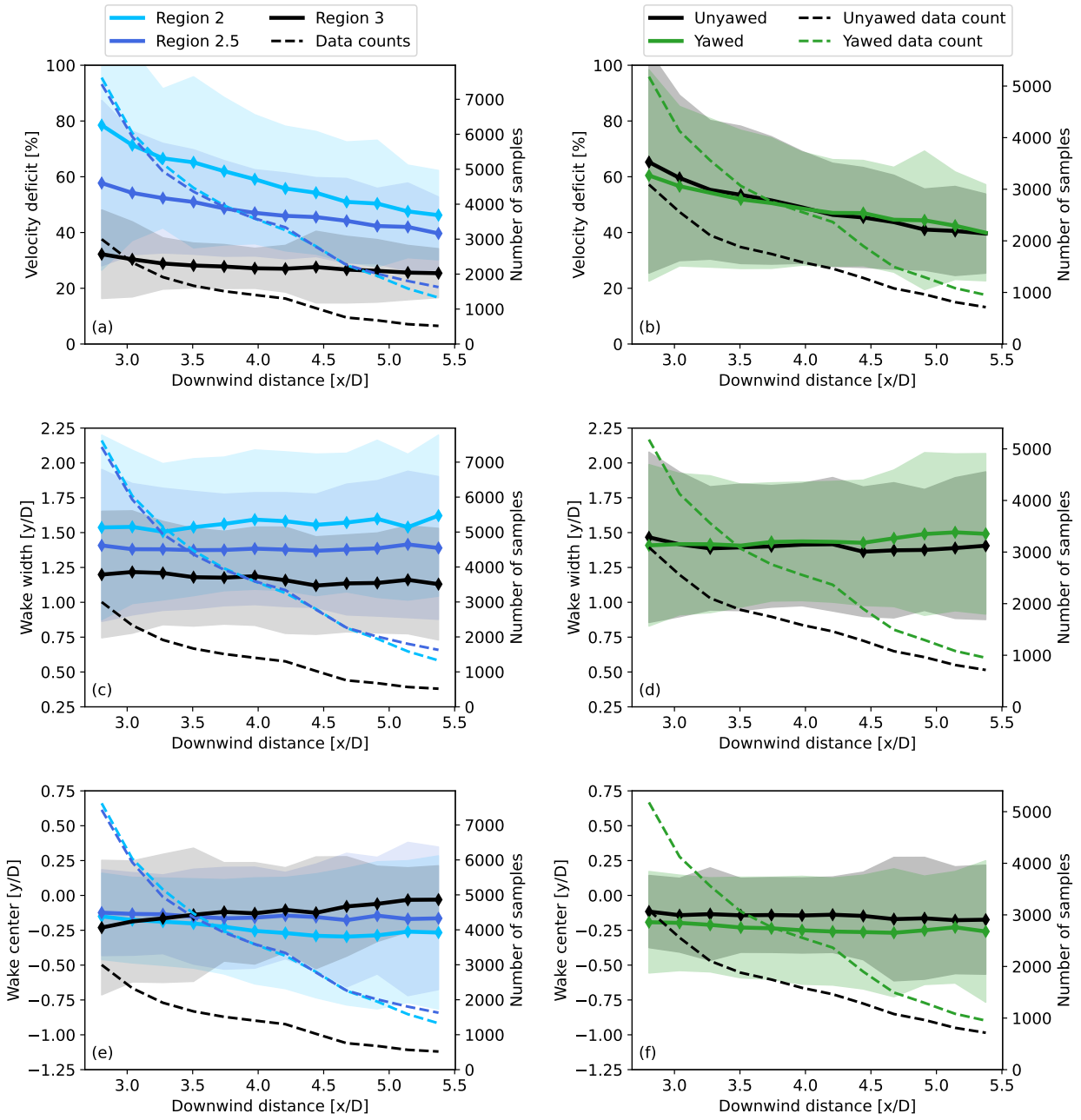

Figure 12. (a, c, e) Wake behavior for all cases under different turbine operating regions, and (b, d, f) a comparison of yawed and unyawed behavior for cases occurring in Regions 2 and 2.5. Note that yawing was inactive in turbine operating Region 3, so the corresponding unyawed data are omitted from the comparison. Any statistically significant differences are highlighted at each range gate with a diamond marker.

4.2 Wake Characteristics As a Function of Turbine Operating Condition

When binning measurements of all wakes by operating region (Figure 12a), Region 2 has the highest relative wake deficit, followed by Regions 2.5 and 3. This behavior occurs because relative wake recovery rate is weaker in Region 2 compared to Region 2.5 and 3 (Rhodes and Lundquist 2013). The wake velocity deficits of Region 2 are $\approx 80\%$ and $\approx 50\%$ at $3D$ and $5.3D$ downstream distances, respectively, where Region 3 has velocity deficit of $\approx 35\%$ and $\approx 25\%$ at $3D$ and $5.3D$ downstream distances, respectively. Because yawed cases are included in this analysis, the significant velocity deficit in Region 2 suggests that wake steering can be more effective in Region 2 than in Regions 2.5 and 3 overall.

As wakes in Regions 2 and 2.5 showed the largest relative velocity deficit, we specifically examine the effect of yawing in these conditions (Figure 12b). Furthermore, wake steering was active in Regions 2 and 2.5 only. Yawed wakes consistently show a similar mean velocity deficit with unyawed wakes in Regions 2 and 2.5. There is no large difference in wake recovery between yawed and unyawed wakes as downwind distance increases. The data set includes a larger number of yawed velocity deficits, but both yawed and unyawed deficits decrease with increasing downwind distance.

The wake width and wake center are investigated for each case under yawed and unyawed conditions (Figure 12c–f). The mean wake width of yawed cases is marginally smaller in the near-wake and increases with downwind distances. However, the mean wake width of unyawed cases does not change much with downstream distance compared to yawed cases. Overall, wake widths behave significantly differently depending on turbine alignment, with yawed wake widths increasing more than unyawed wake widths in the far wake region.

The wake centers of the yawed cases change significantly with downstream distance in comparison to unyawed wakes. These findings suggest that wake steering as measured by nacelle-mounted scanning lidar is an effective method to change the direction of flow deficits directly downwind of turbines.

4.3 Wake Deficits As a Function of Atmospheric Stability and Turbulence Intensity

We quantify the effect of wake steering and its sensitivity to atmospheric stratification (Figure 13a). The standard deviations of both yawed and unyawed velocity deficits decrease with increasing downwind distance. In stable conditions, mean velocity deficits of yawed wakes are statistically different than those of unyawed wakes outside of the mid-wake region. Wake deficits are larger in the far-wake region when wake steering is implemented, and smaller in the near-wake region when wake steering is not in use during stable atmospheric stratification.

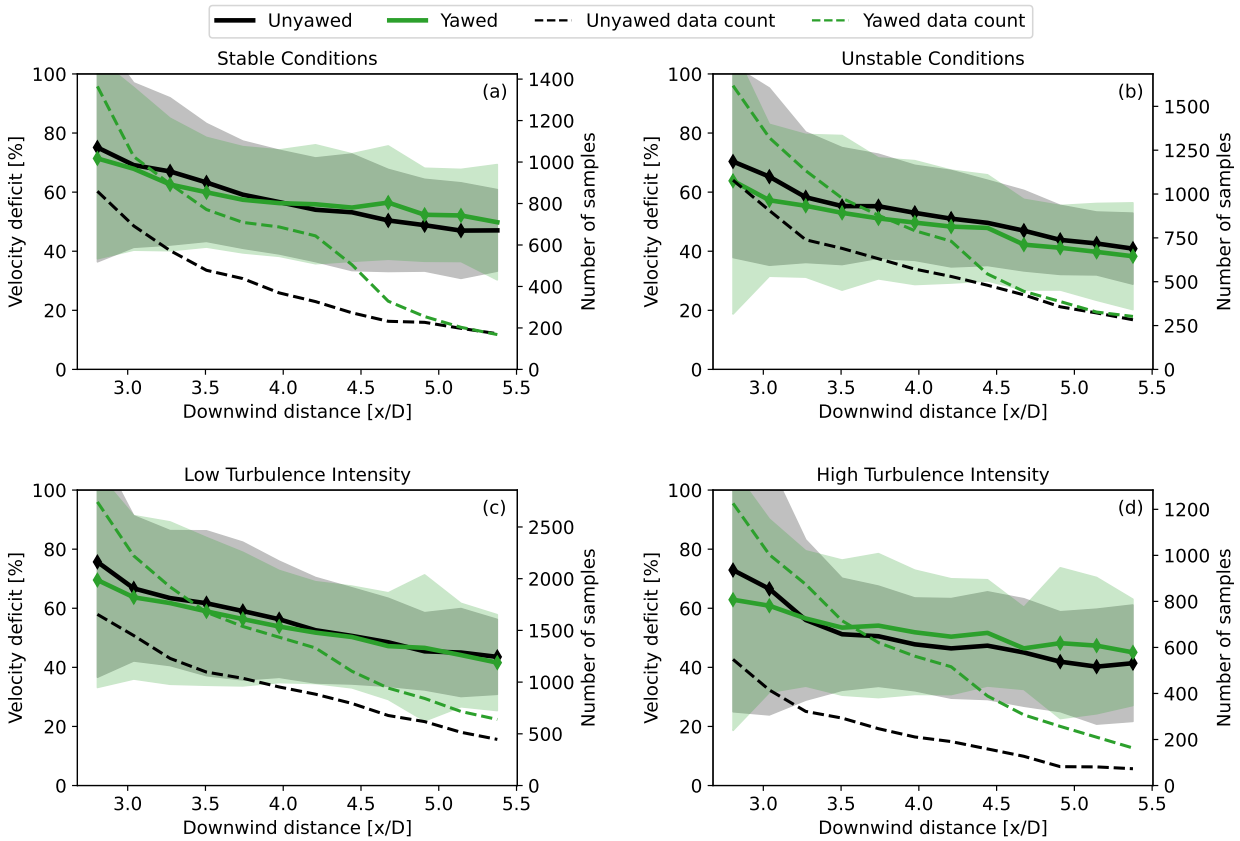

Figure 13. Velocity deficits of yawed and unyawed wakes under (a, b) different atmospheric stability regimes and (c, d) turbulence intensity conditions. Note that solid lines represent the mean of all cases, and dashed lines represent available number of scans. Any statistically significant differences are highlighted at each range gate with a diamond marker.

In unstable conditions (Figure 13b), wake steering has a significant impact on a wake's velocity deficit. Mean velocity deficits are larger when wake steering is not implemented. This behavior suggests that wake steering decreases the degree to which wakes disrupt air flow in unstable atmospheric stratification.

Both yawed and unyawed wake velocity deficits persist farther downstream in stable atmospheric conditions compared to unstable conditions. In the near wake region, yawed wake velocity deficits are $\approx 71\%$ and $\approx 65\%$ in stable and unstable atmospheric conditions respectively, and unyawed wake velocity deficits are $\approx 76\%$ and $\approx 70\%$ in stable and unstable atmospheric conditions respectively. In stable atmospheric conditions, velocity deficits are $\approx 52\%$ and $\approx 50\%$ at $5.3D$ for yawed and unyawed wakes respectively. In unstable atmospheric conditions, velocity deficits are lower on average at $\approx 40\%$ and $\approx 42\%$ at $5.3D$ for yawed and unyawed wakes respectively.

Low-TI conditions tend to occur during stable stratification; thus, low-TI wakes (Figure 13c) generally resemble stable wakes. However, high-TI wakes (Figure 13d) behave slightly different from unstable wakes, despite the similarity in atmospheric condition. In both the far-wake and the near-wake regions, wake velocity deficits are statistically dissimilar whether turbines are yawed or unyawed in unstable stratification. This is also found to be true between yawed and unyawed wakes in high-TI conditions, however yawed wakes do not recover as quickly as they do in unstable atmospheric stratification.

Velocity deficits can vary when comparing across stabilities or turbulence intensities. Yawed wakes have distinct mean velocity deficits when compared in stable versus unstable conditions or low-TI versus high-TI conditions. For example, the velocity deficits at $3D$ downstream are $\approx 70\%$ for low-TI cases (Figure 13c) and $\approx 65\%$ for high-TI cases (Figure 13d). Yawed velocity deficits at $3D$ are $\approx 75\%$ for the stable case (Figure 13a) and $\approx 65\%$ for the unstable case (Figure 13b). The same pattern of similar behavior occurs for yawed wakes in the far-wake region downstream of $4D$. Partitioning via stability or TI, stable yawed wake velocity deficits are marginally larger than unstable yawed wake velocity deficits. Lastly, yawed wakes overall tend to have similar velocity deficit behavior to unyawed wakes with significant differences occurring mainly unstable atmospheric stratification.

4.4 Wake Widths As a Function of Atmospheric Stability and Turbulence Intensity

We quantify the effect of wake steering on wake widths and the sensitivity of wake steering to atmospheric stratification. In stable conditions (Figure 14a), mean widths of yawed wakes are similar to unyawed wakes, growing between $3D$ and $5D$.

In unstable conditions (Figure 14b), wake steering has a larger impact on the width of the wake beyond $4.5D$. Mean wake widths of yawed wakes are significantly larger than unyawed wakes in the far-wake region. This trend appears to diminish close to $5.5D$, suggesting that convective atmospheric mixing may dampen wake steering effects in the very far-wake region.

We notice again that low-TI wakes (Figure 14c) resemble stable wakes. It is statistically evident however that yawed wake widths are larger in the far wake region than unyawed wake widths in low-TI conditions. High-TI wakes (Figure 14d) have slightly different behavior from unstable wakes, with few significant differences occurring before the far wake region. In near-wake low-TI conditions, yawed wake widths resemble unyawed wake widths, just as in stable conditions. In far-wake low-TI conditions, however, yawed wake widths do not trend toward spreading out as much as they do in stable conditions. Mean widths of yawed wakes in high-TI conditions generally mirror the behavior of unyawed wakes, with few significant differences occurring in the near wake region whether wake steering is turned on or off.

4.5 Wake Centerlines As a Function of Atmospheric Stability and Turbulence Intensity

Wake steering affects centerline location, with results dependent on atmospheric stratification (Figure 15a). In stable conditions, yawed wake centerlines are deflected $\approx 0.1D$ away from unyawed wake centerlines at $3D$ downwind. At $4D$ downwind, the mean deflection difference increases to $\approx 0.25D$. Mean centerline locations of yawed wakes deviate from those of unyawed wakes by a quarter rotor diameter close to $4.5D$. Downwind from $4.5D$, yawed wake centerlines continue to deviate farther from their starting point. Centerline deflections between yawed and unyawed cases past $5.3D$ retreat back to $\approx 0.1D$ in difference. This finding suggests that in stable conditions, wake steering affects wake centerline locations in both near- and far-wake regions, but especially from $4D$ to $4.5D$.

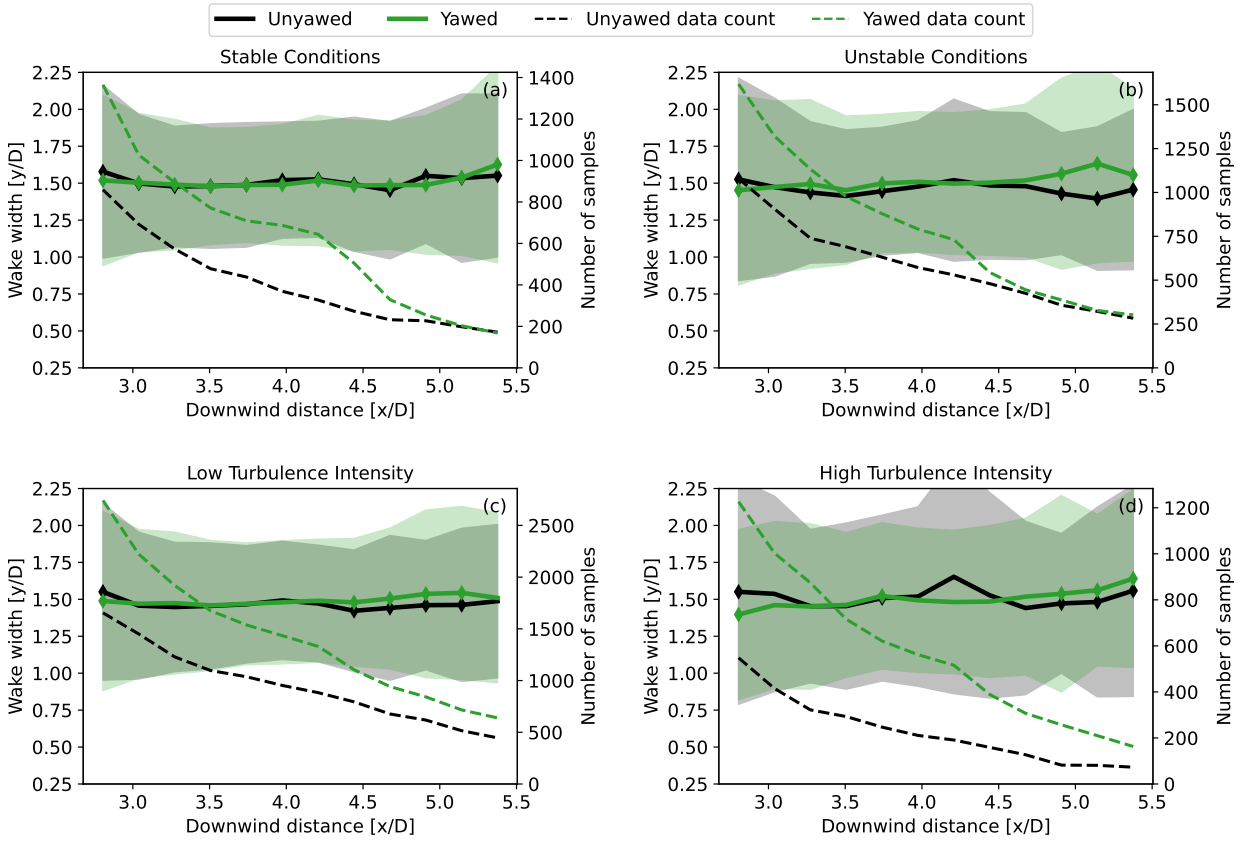

Figure 14. Wake widths of yawed and unyawed wakes under (a, b) different atmospheric stability regimes and (c, d) turbulence intensity conditions. Note that solid lines represent the mean of all cases, and dashed lines represent available number of scans. Any statistically significant differences are highlighted at each range gate with a diamond marker.

However, in unstable conditions (Figure 15b), wake steering has a smaller impact on the centerline of the wake. Mean wake centerlines are still consistently different between $3D$ and $5.3D$ across yawed and unyawed cases. The deflection difference in centerline location between yawed and unyawed wakes is $\approx 0.1D$ in the near wake, $\approx 0.1D$ in the middle wake region, and less than $\approx 0.1D$ in the far-wake region past $5D$. This behavior suggests that convective atmospheric mixing dampens wake steering effects within the near- and far-wake regions. Although these differences are statistically significant, wake steering is more effective in stable conditions, with less deflection in unstable conditions.

The effects of low-TI conditions and stable stratification on wakes are similar. Low-TI wake centers (Figure 15c) resemble stable wake centers. However, the effect of high TI on wakes (Figure 15d) is slightly different than the effect of unstable conditions on wakes. In low-TI conditions, yawed wake centerlines mirror the behavior of unyawed wake centerlines, with larger differences in the midwake region, just as in stable conditions. In high-TI instances, though, this mirrored behavior is not observed. Yawed wake centerlines are deflected farther from unyawed wake centerlines by $\approx 0.1D$ at $3D$ and $\approx 0.35D$ at $4.7D$, suggesting that wake steering is marginally effective in high-TI conditions, while it is not as effective in unstable conditions.

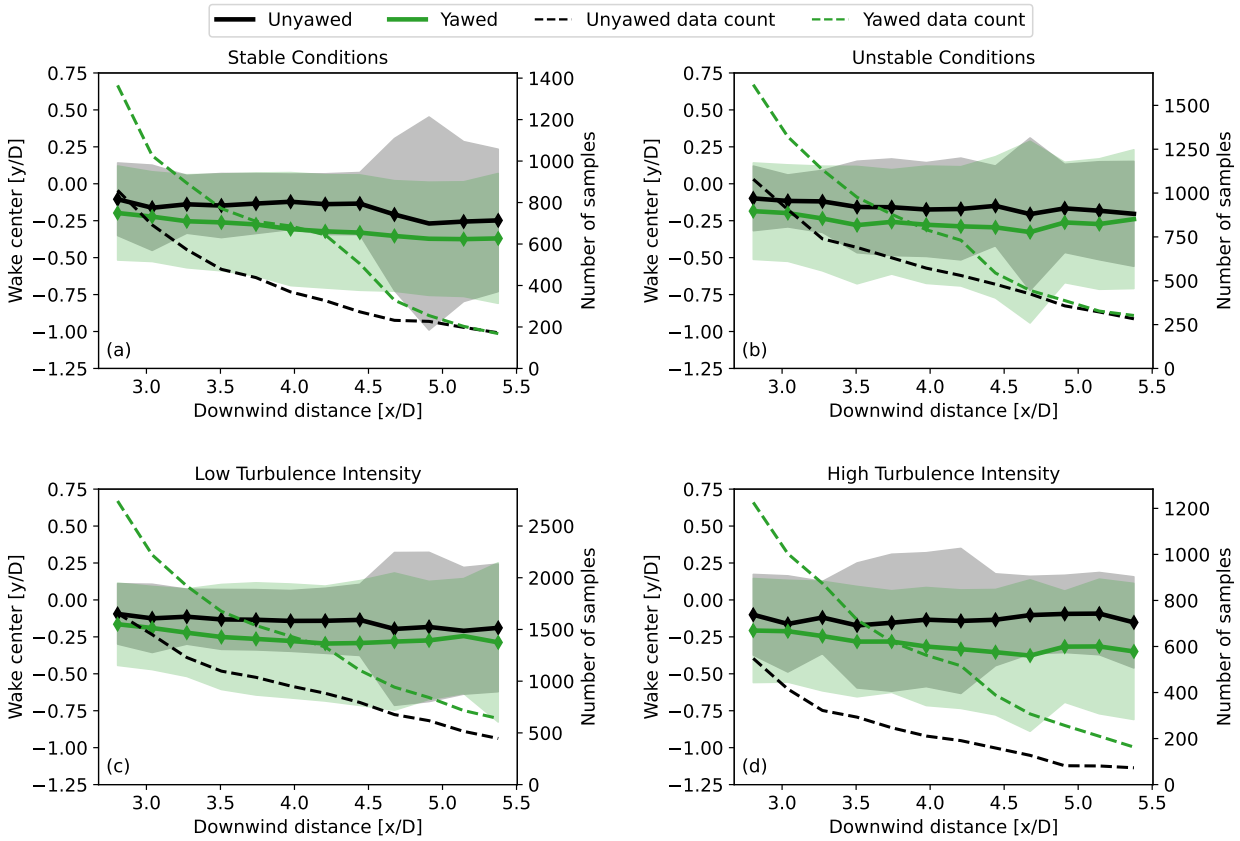

Figure 15. Wake centers of yawed and unyawed wakes under (a) stable atmospheric conditions, (b) unstable atmospheric conditions, (c) low turbulence intensity, and (d) high turbulence intensity. Solid lines represent the mean of all cases, and dashed lines represent available number of scans. Any statistically significant differences are highlighted at each range gate with a diamond marker.

5 Discussion and Conclusions

Using nacelle-mounted lidar scans of wakes, this study quantifies the behavior of yawed and unyawed wind turbine wakes under varying atmospheric conditions. Yawing the turbine away from the mean wind direction effectively deflects wake centerlines, even though yawed wakes have similar width and velocity deficit characteristics when compared to unyawed wakes. We find overall that wake steering is more effective in stable atmospheric and less turbulent stratification, whereas convective atmospheric mixing tends to weaken the desired effect. We do find however that yawing turbines in unstable atmospheric conditions tends to dampen wake velocity deficits. Higher range gate resolution scans fixed at varying elevation angles may be able to provide an insight into quantifying more aspects of turbine wakes, such as wake meander and precise centerline location.

The methods for observing, modeling, and quantifying steered wakes in different atmospheric boundary layer conditions are detailed in this work. Nacelle-mounted lidar scans capture wake velocity deficits, widths, and centerlines to provide detailed observations of wake behaviors. A met tower measures the boundary layer conditions in the atmosphere. From these measurements, we classify atmospheric conditions and group wakes to be studied under the respective atmospheric states they were captured in. Additionally, wakes are grouped by their alignment status to separate yawed and unyawed cases.

A Gaussian curve fit is used to model the wakes' shapes and characteristics. To get realistic wake and ambient wind speeds, the data are filtered based on whether or not the wake width from the fitted model outputs a realistic value. For near-wake and yawed cases, there may be situations where scans are not wide enough to capture the ambient wind speeds surrounding the wakes, so normal distribution curve fitting can be wrong for these situations. This model is then used to quantify wake behavior in different atmospheric conditions.

This study motivates the need for further validation campaigns to uncover more aspects of yawed and unyawed turbine wake behaviors such as precise wake centerline location and wake meander. Lidar scans that span a wider range of azimuth angles would enable characterization of wakes in the near-wake region. Further validation campaigns will be required to give a more precise understanding of the broader implications that wake steering may have as a viable method to mitigate downwind losses on commercial wind plants.

References

Abkar, M., A. Sharifi, and F. Porté-Agel. 2016. "Wake flow in a wind farm during a diurnal cycle" [in en]. *Journal of Turbulence* 17, no. 4 (April): 420–441. ISSN: 1468-5248, accessed October 20, 2021. https://doi.org/10.1080/14685248.2015.1127379. http://www.tandfonline.com/doi/full/10.1080/14685248.2015.1127379.

Ahmad, T., A. Basit, M. Ahsan, O. Coupiac, N. Girard, B. Kazemtabrizi, and P. C. Matthews. 2019. "Implementation and Analyses of Yaw Based Coordinated Control of Wind Farms." *Energies* 12, no. 7 (January): 1266. ISSN: 1996-1073. https://doi.org/10.3390/en12071266.

Aitken, M. L., R. M. Banta, Y. L. Pichugina, and J. K. Lundquist. 2014. "Quantifying Wind Turbine Wake Characteristics from Scanning Remote Sensor Data" [in en]. *Journal of Atmospheric and Oceanic Technology* 31, no. 4 (April): 765–787. ISSN: 0739-0572, 1520-0426, accessed October 26, 2021. https://doi.org/10.1175/JTECH-D-13-00104.1. http://journals.ametsoc.org/doi/10.1175/JTECH-D-13-00104.1.

Aitken, M. L., and J. K. Lundquist. 2014. "Utility-Scale Wind Turbine Wake Characterization Using Nacelle-Based Long-Range Scanning Lidar." *Journal of Atmospheric and Oceanic Technology* 31, no. 7 (April): 1529–1539. ISSN: 0739-0572, accessed February 7, 2017. https://doi.org/10.1175/JTECH-D-13-00218.1. http://journals.ametsoc.org/doi/abs/10.1175/JTECH-D-13-00218.1.

Archer, C. L., and A. Vasel-Be-Hagh. 2019. "Wake steering via yaw control in multi-turbine wind farms: Recommendations based on large-eddy simulation" [in en]. *Sustainable Energy Technologies and Assessments* 33 (June): 34–43. ISSN: 22131388, accessed October 20, 2021. https://doi.org/10.1016/j.seta.2019.03.002. https://linkinghub.elsevier.com/retrieve/pii/S2213138818306544.

Barthelmie, R. J., K. Hansen, S. T. Frandsen, O. Rathmann, J. G. Schepers, W. Schlez, J. Phillips, et al. 2009. "Modelling and measuring flow and wind turbine wakes in large wind farms offshore" [in en]. *Wind Energy* 12, no. 5 (July): 431–444. ISSN: 10954244, 10991824, accessed October 25, 2021. https://doi.org/10.1002/we.348. https://onlinelibrary.wiley.com/doi/10.1002/we.348.

Bastankhah, M., and F. Porté-Agel. 2015. "A wind-tunnel investigation of wind-turbine wakes in yawed conditions" [in en]. *Journal of Physics: Conference Series* 625 (June): 012014. ISSN: 1742-6588, 1742-6596, accessed October 20, 2021. https://doi.org/10.1088/1742-6596/625/1/012014. https://iopscience.iop.org/article/10.1088/1742-6596/625/1/012014.

———. 2016. "Experimental and Theoretical Study of Wind Turbine Wakes in Yawed Conditions." *Journal of Fluid Mechanics* 806 (November): 506–541. ISSN: 0022-1120, 1469-7645. https://doi.org/10.1017/jfm.2016.595.

Bastankhah, M., C. R. Shapiro, S. Shamsoddin, D. F. Gayme, and C. Meneveau. 2022. "A Vortex Sheet Based Analytical Model of the Curled Wake behind Yawed Wind Turbines." *Journal of Fluid Mechanics* 933 (February). ISSN: 0022-1120, 1469-7645. https://doi.org/10.1017/jfm.2021.1010.

Bodini, N., D. Zardi, and J. K. Lundquist. 2017. "Three-dimensional structure of wind turbine wakes as measured by scanning lidar" [in en]. *Atmospheric Measurement Techniques* 10, no. 8 (August): 2881–2896. ISSN: 1867-8548, accessed February 24, 2021. https://doi.org/10.5194/amt-10-2881-2017. https://amt.copernicus.org/articles/10/2881/2017/.

Brugger, P., M. Debnath, A. Scholbrock, P. Fleming, P. Moriarty, E. Simley, D. Jager, et al. 2020. "Lidar measurements of yawed-wind-turbine wakes: characterization and validation of analytical models" [in en]. *Wind Energy Science* 5, no. 4 (October): 1253–1272. ISSN: 2366-7451, accessed October 20, 2021. https://doi.org/10.5194/wes-5-1253-2020. https://wes.copernicus.org/articles/5/1253/2020/.

Damiani, R., S. Dana, J. Annoni, P. Fleming, J. Roadman, J. van Dam, and K. Dykes. 2018. "Assessment of wind turbine component loads under yaw-offset conditions." *Wind Energy Science* 3 (1): 173–189. https://doi.org/10.5194/wes-3-173-2018.

Doekemeijer, B. M., S. Kern, S. Maturu, S. Kanev, B. Salbert, J. Schreiber, F. Campagnolo, et al. 2021. "Field Experiment for Open-Loop Yaw-Based Wake Steering at a Commercial Onshore Wind Farm in Italy." *Wind Energy Science* 6, no. 1 (January): 159–176. ISSN: 2366-7443. https://doi.org/10.5194/wes-6-159-2021.

Fleming, P., J. Annoni, M. Churchfield, L. A. Martinez-Tossas, K. Gruchalla, M. Lawson, and P. Moriarty. 2018. "A simulation study demonstrating the importance of large-scale trailing vortices in wake steering." *Wind Energy Science* 3 (1): 243–255. https://doi.org/10.5194/wes-3-243-2018.

Fleming, P., J. King, E. Simley, J. Roadman, A. Scholbrock, P. Murphy, J. K. Lundquist, et al. 2020. "Continued results from a field campaign of wake steering applied at a commercial wind farm – Part 2." *Wind Energy Science* 5 (3): 945–958. https://doi.org/10.5194/wes-5-945-2020.

Fleming, P., J. Annoni, J. J. Shah, L. Wang, S. Ananthan, Z. Zhang, K. Hutchings, P. Wang, W. Chen, and L. Chen. 2017a. "Field test of wake steering at an offshore wind farm" [in en]. *Wind Energy Science* 2, no. 1 (May): 229–239. ISSN: 2366-7451, accessed October 16, 2021. https://doi.org/10.5194/wes-2-229-2017. https://wes.copernicus.org/articles/2/229/2017/.

———. 2017b. "Field Test of Wake Steering at an Offshore Wind Farm." *Wind Energy Science* 2, no. 1 (May): 229–239. ISSN: 2366-7443. https://doi.org/10.5194/wes-2-229-2017.

Fleming, P., J. King, K. Dykes, E. Simley, J. Roadman, A. Scholbrock, P. Murphy, et al. 2019. "Initial results from a field campaign of wake steering applied at a commercial wind farm – Part 1" [in en]. *Wind Energy Science* 4, no. 2 (May): 273–285. ISSN: 2366-7451, accessed October 16, 2021. https://doi.org/10.5194/wes-4-273-2019. https://wes.copernicus.org/articles/4/273/2019/.

Howland, M. F., C. M. González, J. J. P. Martínez, J. B. Quesada, F. P. Larrañaga, N. K. Yadav, J. S. Chawla, and J. O. Dabiri. 2020. "Influence of atmospheric conditions on the power production of utility-scale wind turbines in yaw misalignment" [in en]. *Journal of Renewable and Sustainable Energy* 12, no. 6 (November): 063307. ISSN: 1941-7012, accessed October 20, 2021. https://doi.org/10.1063/5.0023746. http://aip.scitation.org/doi/10.1063/5.0023746.

Howland, M. F., S. K. Lele, and J. O. Dabiri. 2019. "Wind Farm Power Optimization through Wake Steering." *Proceedings of the National Academy of Sciences* 116, no. 29 (July): 14495–14500. https://doi.org/10.1073/pnas.1903680116.

King, J., P. Fleming, R. King, L. A. Martínez-Tossas, C. J. Bay, R. Mudafort, and E. Simley. 2021. "Control-Oriented Model for Secondary Effects of Wake Steering." *Wind Energy Science* 6, no. 3 (May): 701–714. ISSN: 2366-7443. https://doi.org/10.5194/wes-6-701-2021.

Lee, J. C. Y., and M. J. Fields. 2021. "An Overview of Wind-Energy-Production Prediction Bias, Losses, and Uncertainties." *Wind Energy Science* 6, no. 2 (March): 311–365. ISSN: 2366-7443. https://doi.org/10.5194/wes-6-311-2021.

Lissaman, P. B. S. 1979. "Energy Effectiveness of Arbitrary Arrays of Wind Turbines." *Journal of Energy* 3 (6): 323–328. ISSN: 0146-0412. https://doi.org/10.2514/3.62441. https://doi.org/10.2514/3.62441.

Machefaux, E., G. C. Larsen, T. Koblitz, N. Troldborg, M. C. Kelly, A. Chougule, K. S. Hansen, and J. S. Rodrigo. 2016. "An experimental and numerical study of the atmospheric stability impact on wind turbine wakes: Experimental and numerical study of the atmospheric stability impact on wake" [in en]. *Wind Energy* 19, no. 10 (October): 1785–1805. ISSN: 10954244, accessed October 20, 2021. https://doi.org/10.1002/we.1950. https://onlinelibrary.wiley.com/doi/10.1002/we.1950.

Martínez-Tossas, L. A., J. Annoni, P. A. Fleming, and M. J. Churchfield. 2019. "The Aerodynamics of the Curled Wake: A Simplified Model in View of Flow Control." *Wind Energy Science* 4, no. 1 (March): 127–138. ISSN: 2366-7443. https://doi.org/10.5194/wes-4-127-2019.

Meyers, J., C. Bottasso, K. Dykes, P. Fleming, P. Gebraad, G. Giebel, T. Göçmen, and J.-W. van Wingerden. 2022. "Wind Farm Flow Control: Prospects and Challenges." *Wind Energy Science Discussions* (March): 1–56. ISSN: 2366-7443. https://doi.org/10.5194/wes-2022-24.

Murphy, P., J. K. Lundquist, and P. Fleming. 2020. "How wind speed shear and directional veer affect the power production of a megawatt-scale operational wind turbine" [in en]. *Wind Energy Science* 5, no. 3 (September): 1169–1190. ISSN: 2366-7451, accessed October 20, 2021. https://doi.org/10.5194/wes-5-1169-2020. https://wes.copernicus.org/articles/5/1169/2020/.

Nouri, R., A. Vasel-Be-Hagh, and C. L. Archer. 2020. "The Coriolis force and the direction of rotation of the blades significantly affect the wake of wind turbines." *Applied Energy* 277:115511. ISSN: 0306-2619. https://doi.org/https://doi.org/10.1016/j.apenergy.2020.115511.

NREL. 2021. *FLORIS. Version 2.4.0.* https://github.com/NREL/floris.

Park, S., L. Linsen, O. Kreylos, J. Owens, and B. Hamann. 2006. "Discrete Sibson interpolation." *IEEE Transactions on Visualization and Computer Graphics* 12 (2): 243–253. https://doi.org/10.1109/TVCG.2006.27.

Porté-Agel, F., M. Bastankhah, and S. Shamsoddin. 2020. "Wind-Turbine and Wind-Farm Flows: A Review" [in en]. *Boundary-Layer Meteorology* 174, no. 1 (January): 1–59. ISSN: 0006-8314, 1573-1472, accessed October 20, 2021. https://doi.org/10.1007/s10546-019-00473-0. http://link.springer.com/10.1007/s10546-019-00473-0.

Rhodes, M. E., and J. K. Lundquist. 2013. "The effect of wind-turbine wakes on summertime US Midwest atmospheric wind profiles as observed with ground-based Doppler lidar." *Boundary-layer meteorology* 149 (1): 85–103.

Sengers, B. A. M., M. Zech, P. Jacobs, G. Steinfeld, and M. Kühn. 2022. "A Physically Interpretable Data-Driven Surrogate Model for Wake Steering." *Wind Energy Science* 7, no. 4 (July): 1455–1470. ISSN: 2366-7443. https://doi.org/10.5194/wes-7-1455-2022.

Shapiro, C. R., D. F. Gayme, and C. Meneveau. 2018. "Modelling Yawed Wind Turbine Wakes: A Lifting Line Approach." *Journal of Fluid Mechanics* 841 (April). ISSN: 0022-1120, 1469-7645. https://doi.org/10.1017/jfm.2018.75.

Shapiro, C. R., G. M. Starke, C. Meneveau, and D. F. Gayme. 2019. "A Wake Modeling Paradigm for Wind Farm Design and Control." *Energies* 12, no. 15 (January): 2956. ISSN: 1996-1073. https://doi.org/10.3390/en12152956.

Siemens Gamesa Renewable Energy. 2019. *Siemens Gamesa Now Able to Actively Dictate Wind Flow at Offshore Wind Locations.* https://www.siemensgamesa.com/en-int/newsroom/2019/11/191126-siemens-gamesa-wake-adapt-en.

Simley, E., P. Fleming, N. Girard, L. Alloin, E. Godefroy, and T. Duc. 2021. "Results from a Wake-Steering Experiment at a Commercial Wind Plant: Investigating the Wind Speed Dependence of Wake-Steering Performance." *Wind Energy Science* 6, no. 6 (November): 1427–1453. ISSN: 2366-7443. https://doi.org/10.5194/wes-6-1427-2021.

Thomson, K., and P. Sorensen. 1999. "Fatigue loads for wind turbines operating in wakes." *Journal of Wind Engineering and Industrial Aerodynamics* 80, nos. 1-2 (March): 121–136. https://doi.org/10.1016/S0167-6105(98)00194-9.

Vanderwende, B. J., and J. K. Lundquist. 2012. "The modification of wind turbine performance by statistically distinct atmospheric regimes." *Environmental Research Letters* 7, no. 3 (September): 034035. ISSN: 1748-9326, accessed October 2, 2015. https://doi.org/10.1088/1748-9326/7/3/034035. http://stacks.iop.org/1748-9326/7/i=3/a=034035?key=crossref.4176c6d3737cf5968f48c522fee7f51e.

Vollmer, L., G. Steinfeld, D. Heinemann, and M. Kühn. 2016. "Estimating the wake deflection downstream of a wind turbine in different atmospheric stabilities: an LES study" [in en]. *Wind Energy Science* 1, no. 2 (September): 129–141. ISSN: 2366-7451, accessed January 3, 2022. https://doi.org/10.5194/wes-1-129-2016. https://wes.copernicus.org/articles/1/129/2016/.

Wang, H., R. J. Barthelmie, A. Clifton, and S. C. Pryor. 2015. "Wind Measurements from Arc Scans with Doppler Wind Lidar" [in en]. *Journal of Atmospheric and Oceanic Technology* 32, no. 11 (November): 2024–2040. ISSN: 0739-0572, 1520-0426, accessed October 20, 2021. https://doi.org/10.1175/JTECH-D-14-00059.1. https://journals.ametsoc.org/view/journals/atot/32/11/jtech-d-14-00059_1.xml.

Wingerden, J. W. van, P. A. Fleming, T. Göçmen, I. Eguinoa, B. M. Doekemeijer, K. Dykes, M. Lawson, et al. 2020. "Expert Elicitation on Wind Farm Control." *Journal of Physics: Conference Series* 1618, no. 2 (September): 022025. ISSN: 1742-6596. https://doi.org/10.1088/1742-6596/1618/2/022025.

Wu, Y.-T., and F. Porté-Agel. 2012. "Atmospheric Turbulence Effects on Wind-Turbine Wakes: An LES Study" [in en]. *Energies* 5, no. 12 (December): 5340–5362. ISSN: 1996-1073, accessed October 15, 2021. https://doi.org/10.3390/en5125340. http://www.mdpi.com/1996-1073/5/12/5340.